Power Allocation and 3-D Placement for Floating Relay Supporting Indoor Communications

Yue Li, Guangsheng Feng, Mohammad Ghasemiahmadi, and Lin Cai, *Senior Member, IEEE*

Abstract—With the rapid development of mobile Internet and urban constructions, high-volume and dynamic indoor communications bring challenges to cellular systems. High penetration loss and deep shadowing channels of indoor users may substantially degrade the transmission efficiency and system throughput. To address this issue, this paper proposes a solution using Floating Relay (FR) given the mature technologies of unmanned aerial vehicle (UAV). We target the undesirable channel conditions of indoor users, introduce the FR into the cellular system to improve transmission efficiency and maximize system throughput. Considering the capacity limit of the FR's back-haul link and the maximum transmission power of each user, an optimization problem is formulated to maximize the system throughput. The optimal power allocation strategy is then obtained for each user, and two effective online 3-D placement algorithms are proposed for the FR to approach the optimal location in the unpredictable and predictable scenarios, respectively. Extensive simulations are conducted. The achieved maximum system throughput, convergence rate, and accumulated throughput are used to evaluate the proposed algorithms. According to the comparisons between the two proposed algorithms and with off-line schemes, they show superiorities in their targeted scenarios, respectively.

Index Terms—Indoor communication, 3-D, floating relay, UAV, power allocation, 3-D placement

1 Introduction

With the rapid development of mobile Internet and urban constructions, high-volume and dynamic indoor communications bring new challenges to cellular systems. An indoor cellular user needs to communicate with its serving base station (BS) which typically locates outdoors, and thus the communication channel may suffer from high penetration loss and high shadowing [1], [2], which may substantially degrade the transmission efficiency and system throughput.

In this paper, we focus on the urban area full of high-rise buildings, e.g., business and commercial districts, where both users and existing BSs are 3-D distributed. Introducing new small cells for indoor users may not be helpful due to the difficulties and cost of the BS deployment in this scenario. The optimal location of a new BS to cover the users in upper floors of skyscrapers may be in the mid-air and people are more sensitive to the radiation from a BS. Furthermore, people may gather at different places, such as cafeteria, meeting room, and lobby, at different time. A traditional BS with fixed location cannot provide a dynamic coverage for the moving crowd in the building.

To address the above challenge, we propose an alternative approach using unmanned aerial vehicle (UAV), which had become mature in terms of lighter, more flexible and having a longer battery life [3]. We propose to use a UAV carrying a relay node, so we can incorporate Floating Relay (FR) in the cellular system. The FR can move towards the indoor users to compensate their channels and increase the transmission efficiency. It can also adjust the position according to the real-time traffic and the distribution of users' locations. Thanks to its 3-D mobility, the coverage offered by an FR may be much larger than that of a single small cell. Therefore, the cost of deploying new small cells can be greatly reduced.

However, how to find the optimal location of the FR and, accordingly, allocate users' transmission power to achieve the best system performance in the cellular network remain open, which motivates this work. The main contributions of this paper are summarized as follows:

- Considering the capacity limit of FR's back-haul link and the maximum transmission power of each user, an optimization problem is formulated to maximize the system throughput.
- The optimal power allocation strategy, i.e., how to allocate the transmission power of each user for its existing serving BS and the FR, is derived. The maximum system throughput can be achieved given the location of the FR.
- Based on the optimal power allocation, two effective online 3-D placement algorithms with low complexity are proposed for the FR to find the optimal location in unpredictable and predictable scenarios, respectively.
- Extensive simulations are conducted. The achieved maximum system throughput, convergence rate,

- *Y. Li, M. Ghasemiahmadi, and L. Cai are with the Department of Electrical and Computer Engineering, University of Victoria, Victoria, BC V8P 5C2, Canada. E-mail: {liyue331, ghasemi}@uvic.ca, cai@ece.uvic.ca.*
- *G. Feng is with the College of Computer Science and Technology, Harbin Engineering University, Haerbin, Heilongjiang 150001, China. E-mail: fengguangsheng@hrbeu.edu.cn.*

Manuscript received 5 Apr. 2017; revised 29 Mar. 2018; accepted 20 May 2018. Date of publication 28 May 2018; date of current version 4 Feb. 2019. (Corresponding author: Lin Cai.)
For information on obtaining reprints of this article, please send e-mail to: reprints@ieee.org, and reference the Digital Object Identifier below.
Digital Object Identifier no. 10.1109/TMC.2018.2840989

and accumulated throughput are used to evaluate the proposed algorithms. Comparing to the off-line schemes, the proposed algorithms show superiorities in their targeted scenarios, respectively.

The rest of paper is organized as follows. In Section 2, the related work is described. Section 3 presents the system model. Given a fixed location of the FR, the optimal power allocation strategy for each User Equipment (UE) corresponding to the maximum system throughput is derived in Section 4, based on which, two 3-D placement algorithms targeting on different scenarios are proposed in Section 5. Performance analysis is given in Section 6, followed by future directions and the concluding remarks in Sections 7 and 8, respectively.

2 Related Work

The idea of applying moving network node went back to 1998. A US patent by. Gavrilovich [4] required base stations to move along a roadway to provide coverage for vehicles. The recent ones include the Project Loon [5] led by Google, where an LTE base station is carried by a balloon to provide the Internet access in rural and remote areas. Facebook has also launched Aquila to expand the Internet's reach [6]. The Flying Ubiquitous Sensor Networks (FUSN) [7] combined aerial devices and communication-capable nodes.

Many optimization problems related to mobile sinks in the Wireless Sensor Networks (WSNs) have been formulated and solved in the literature, among which balanced energy consumption is a main objective. Routing methods, data collection strategies, and the optimal deployment were proposed in [8], [9], [10], [11], [12], [13] to increase the network lifetime. The trade-off between energy saving and traffic delay was analyzed in [14]. The mobile data collection process is modelled by an $M/G/1/c$ queuing system with the discipline of nearest-job-next in [15]. Akbar et al. [16] focused on the 3-D underwater scenario and proposed an efficient data collection scheme to improve the lifetime, throughput, and delay. However, only linear route of the mobile sink was considered. Besides lifetime, transmission efficiency and connectivity can also be improved by moving network nodes [17]. Bekmezci et al. [18] provided a comprehensive survey on Flying Ad-hoc NETwork (FANET). The MASP scheme was proposed in [19] to increase the amount of collected data given the same energy consumption. In [20], authors implemented a Mobile Ad-hoc NETwork (MANET) to collect or disseminate content in complicated terrain. The system was then found useful in urban scenarios because of the existence of Line Of Sight (LOS) channels between Micro Air Vehicles (MAVs). This test was done by using eBee devices [21]. Shallcross and van den Berg [22] proposed an algorithm placing a specified number of relay nodes to create a spanning network that minimizes the maximum link length. In [23], a multi-hop network was formed by the UAVs and thus provided connections between isolated sensor nodes and the base station. This work mainly focused on how to maintain the connectivity of the UAV-network.

Besides the WSN and the IEEE 802.11 protocols, the UAV in a cellular system was considered in [24]. The project Loon was based on the LTE system, but the movement of a balloon cannot be dynamic so that the application scenario was restricted to the macro coverage extension for remote areas. The link level analysis based on the Nakagami fading model was given in [25], where the mobile relay was fixed on a train. Lyu et al. [26] studied a wireless system where the UAV flies above distributed ground terminals, but the network topology was one-dimensional, and the flight path of the UAV was predetermined. In [27], [28], use cases and applications of UAV-aided wireless communications, i.e., UAV-aided ubiquitous coverage, UAV-aided relaying, and UAV-aided information dissemination and data collection, were discussed. Alzenad et al. [29], Bor-Yaliniz et al. [30], Mozaffari et al. [31] focused on maximizing the number of covered users. Mozaffari et al. [32] adopted the same objective and further assumed an under-laid D2D network without considering the coverage and capacity limits of the existing BSs and the back-haul. The connection between the UAV and BSs was considered in [33] for coverage optimization, where a UE shall connect to either the BS or the UAV, not both. Besides coverage, energy consumption is another popular metric. Devices' energy consumption was optimized in [34] and [35], where the UAV was used to collect IoT packets. The propulsion energy consumption of the UAV was analyzed and an energy-efficient trajectory design was proposed in [36]. Given the increasing traffic demand, the capacity (or throughput) of the cellular system desires further improvement. The UAV was applied to facilitate the transmission between one pair of nodes, and the throughput was maximized for the pair [37]. The downlink throughput was optimized in [38], where the UAV flew at a fixed altitude and users cannot connect to both the UAV and BS at the same time.

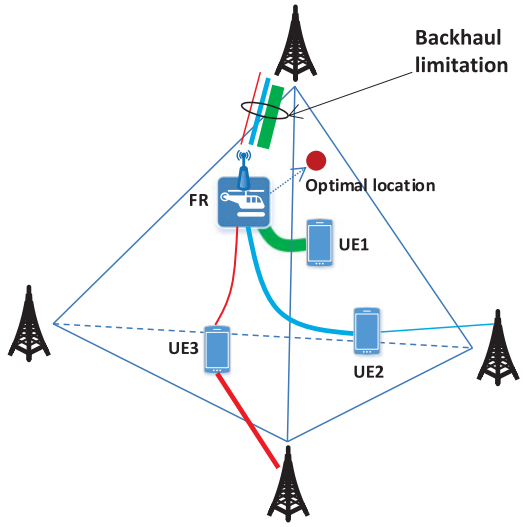

Fig. 1. The floating relay with back-haul limit.

Different from the above work, in this paper, we focus on maximizing the system throughput while considering the capacity limit of the back-haul link and users' transmission power constraint. Each user can connect to the FR and its serving BS simultaneously. How to efficiently allocate user's transmission power among two radio links and find the optimal location of the FR are open issues to be addressed.

3 System Model

Fig. 1 gives an example of the system model. There are several existing BSs and UEs in a 3-D space. A UE shall connect

to the serving BS providing the best average channel quality considering path loss and shadowing. Given the current location of the FR, each UE divides its transmission power into two parts: one is to communicate with the FR and the other is to the serving BS. The objective is to maximize the system throughput. Assuming that the UEs' power allocations are controlled by the network in a centralized way, we investigate the optimal power allocation strategy and the optimal location for the FR.

We denote the link between a UE and the FR as a front-haul link, and the one between a UE and its serving BS as a serving link. The maximum throughput of each single UE is not the objective of power allocation between front-hauls and serving links, because the sum of front-hauls' data rate may exceed the back-haul's capacity. Due to this limit, UEs' power allocations are correlated to each other. The optimal solution is to maximize the system throughput, i.e., the sum of the data rates of all the UEs' front-haul links and serving links, rather than a single UE's throughput.

We use link capacity, denoted by $C(d,p)$, to approximate the link data rate in this paper. It is the Shannon capacity of a link given the transmission power p and distance d

$$C(d,p) = W \log_2\left(1+\frac{p\cdot g(d)}{N_0}\right), \tag{1}$$

where $g(d)$ is the channel and antenna gain, and N_0 is the power of noise. We do not consider the effect of fast fading because it is difficult to react according to fast fading. The channel gain is given by $g(d) = d^{-r}\Psi/K_0$, where r is the path loss exponent, Ψ represents the shadowing effect, and K_0 is a constant. Considering the nearfield effect, $g(d) = [\max(d, d_0)]^{-r}\Psi/K_0$, where d_0 is the reference distance.

In this paper, the resources are statically allocated to users using orthogonal spectrum. Given the poor channels of indoor users (high penetration loss and possible deep shadowing for users inside buildings), the scheduling and feedback messages need to consume a large portion of the cellular resources to meet the link budget of the control channel, which is much higher than that of the data channel. Thus, the traditional dynamic scheduling may be too costly to apply. Therefore, the Physical Resource Block (PRB) is assigned statically (via high-layer messages) in the proposed solution to reduce the control overhead, so each user has a fixed bandwidth. The result with fixed bandwidth allocation is a valuable baseline, and the performance can be improved if coordinated scheduling between different BSs is possible. We do not specify the multiple access scheme in this paper. As long as each user has orthogonal resources, such as frequency, code, and/or time, they will not interfere with each other.

The UAV broadcasts the reference signal as the Type 1a relay node in the LTE system [39]. The UE shall measure the channels to its serving BS and the FR, respectively, and then report the channel conditions and its locations to the serving BS. Neighboring BSs share the information via wired links (the X2 interface) without occupying any wireless resource. The FR's serving BS collects the information of the FR and UEs in neighboring cells, and then calculates the next move and notifies the FR. Given the procedures above, the overhead will not increase significantly because the UE nevertheless has to measure the channel and report it. Thus, we only increase the payload of the feedback message to include the information of the channel to the FR. Given that each UE's frequency band is statically allocated, the feedback message can be concise. The notification of the FR's next move may only contain a GPS coordinate (including altitude) and be sent once per several seconds.

The location of the FR greatly affects the channel gains of the back-haul and all the front-hauls, and thus the maximum system throughput varies. Our objective, finding the optimal location of the FR, can be formulated as a primal optimization problem (P1) with three constraints as follows:

$$\max_{\boldsymbol{\alpha},\boldsymbol{x}} \sum_{i\in\mathbb{U}} [C(||\boldsymbol{x}-\boldsymbol{u}_i||_2,\alpha_i) + C(||\boldsymbol{s}_i-\boldsymbol{u}_i||_2, P_t-\alpha_i)] \quad \text{(P1)},$$

$$\text{s.t.} \sum_{i\in\mathbb{U}} C(||\boldsymbol{x}-\boldsymbol{u}_i||_2,\alpha_i) \le C'(||\boldsymbol{x}-\boldsymbol{s}_x||_2, P_t^F, \beta), \quad \text{(C1)}$$

$$\alpha_i \le P_t, \ \ \forall i\in\mathbb{U}, \quad \text{(C2)}$$

$$\alpha_i \ge 0, \ \ \forall i\in\mathbb{U}, \quad \text{(C3)}$$

where $\boldsymbol{x}$ is the 3-D coordinate vector (location) of the FR, $\boldsymbol{u}_i$ is the location of the ith UE, $\boldsymbol{s}_i$ and $\boldsymbol{s}_x$ are the locations of the serving BSs selected by the ith UE and the FR, respectively. α_i denotes the transmission power of the ith UE that is allocated to the FR. P_t is the total UE transmission power and P_t^F is that of the FR. $\mathbb{U}$ is the UE set. In this paper, we use the bold font denoting vectors, the double struck font denoting sets.

The constraint (C1) is the back-haul capacity limit, which means that the sum of front-hauls' capacities cannot exceed the back-haul's. β denotes that the bandwidth allocated to the FR's back-haul is β times of UE's bandwidth and $C'(d,p,\beta)$ is given by

$$C'(d,p,\beta) = \beta W \log_2\left(1+\frac{p\cdot g(d)}{\beta N_0}\right). \tag{2}$$

(C2) and (C3) determine the valid range of the power allocated to the FR, which is non-negative and less than the maximum UE transmission power.

The global information is needed to make the decision for the FR's future moves. Since the traffic load and the topology of active nodes are changing (dynamical network), the global information is time-varying. Therefore, the FR may make the decision for either one step ahead given the unpredictable network or several steps ahead given the predictable network, i.e., the network is stable in a certain duration.

In the following sections, (P1) is decoupled and solved case by case. Given a fixed location of the FR, we first develop the optimal power allocation strategy, considering both the back-haul capacity constraint and maximum UE transmission power constraint, to maximize the system throughput. Next, if the network is unpredictable, given the optimal power allocation of each fixed location of the FR, we calculate the direction of the FR's next move. The near-optimal location for the FR can be found by a proposed online iterative algorithm. If the network is predictable, given the stable duration, we find out the near-optimal location within the FR's maximum moving range by a proposed searching algorithm with adaptive step length. Then, the FR move to the converged near-optimal location directly.

4 The Optimal Power Allocations

In this section, given the location of the FR, we obtain the optimal power allocation strategy. The problem (P1) is changed to (P2) as follows:

$$\begin{aligned}
&\max_{\boldsymbol{\alpha}} \ \sum_{i\in\mathbb{U}}[C(d_i,\alpha_i)+C(D_i,P_t-\alpha_i)], && \text{(P2)}\\
&\textbf{s.t.} \ \sum_{i\in\mathbb{U}} C(d_i,\alpha_i)\le C'(D_x,P_t^F,\beta), && \text{(C1)}\\
&\quad \alpha_i\le P_t, \ \ \forall i\in\mathbb{U}, && \text{(C2)}\\
&\quad \alpha_i\ge 0, \ \ \forall i\in\mathbb{U}, && \text{(C3)}
\end{aligned}$$

where d_i and D_i are the distances of the ith UE to the FR and its serving BS, respectively. D_x is the distance from the FR to its serving BS. All the distances are known given the fixed location of the FR. Both the objective function and constraints in (P2) are convex [40].

To solve the problem, we consider different cases and solve them one by one. The constraint (C1) can be separated into two cases, which are back-haul unlimited and back-haul limited, respectively. In the first case, (C1) can be removed; in the second case, (C1) becomes (C1') as shown below:

$$\sum_{i\in\mathbb{U}} C(d_i,\alpha_i)=C'(D_x,P_t^F,\beta). \qquad \text{(C1')}$$

We first focus on the back-haul unlimited case. The constraints (C2) and (C3) define the valid range of the power allocation. α_i with and without these two constraints may result in different front-haul capacities and thus affect the back-haul budget for others. However, given that the back-haul is unlimited, the data rate of each UE's front-haul is independent to others. Thus, the power allocations for UEs are not correlated, and we can find the optimal allocation for each UE individually using (P2'), where the summation in (P2) is removed, subject to (C2) and (C3)

$$\begin{aligned}
&\max_{\alpha_i} \ C(d_i,\alpha_i)+C(D_i,P_t-\alpha_i), \ \ \forall i\in\mathbb{U}. && \text{(P2')}\\
&\textbf{s.t.} \ \text{(C2)}, \text{(C3)}
\end{aligned}$$

Eq. (P2') can be considered as the sum-rate maximization problem for two channel states with sum-power constraint. It is solved as follows. Substituting with (1), the equivalent expression of (P2') is given by

$$\begin{aligned}
&\max_{\alpha_i} \ W\log_2(1+H_{di}\alpha_i)+W\log_2(1+H_{Di}(P_t-\alpha_i))\\
&\Longrightarrow \max_{\alpha_i} \ \ln(1+H_{di}\alpha_i)+\ln(1+H_{Di}(P_t-\alpha_i)), \ \forall i\in\mathbb{U}.
\end{aligned} \qquad (3)$$

Taking a derivative of (3) w.r.t. α_i, and making it equal to zero, we have

$$\begin{aligned}
&\frac{H_{di}}{1+H_{di}\alpha_i}-\frac{H_{Di}}{1+H_{Di}(P_t-\alpha_i)}=0\\
&\Longrightarrow \alpha_i=\frac{H_{di}-H_{Di}+H_{di}H_{Di}P_t}{2H_{di}H_{Di}}, \ \forall i\in\mathbb{U}.
\end{aligned} \qquad (4)$$

The power allocation α_i in (4) is optimal from a UE's perspective. We use α_i^* to denote the optimal power allocation in (P2), $\alpha_i^*=\alpha_i, \ \forall i\in\mathbb{U}$, if the constraints (C1), (C2) and (C3) are all satisfied.

If (C2) and (C3) are not satisfied, we should first draw each $\alpha_i, \forall i\in\mathbb{U}$, back into the valid range, i.e., force the negative ones equal to zero and the ones larger than P_t equal to P_t, respectively. Due to the convexity of (P2'), if α_i calculated by (4) is negative, the maximum system throughput will be monotonically decreased when we increase α_i. Similarly, if we reduce α_i, which is originally larger than P_t, the maximum system throughput is also monotonically decreased. It can be concluded that if the ith UE's power allocation calculated by (4), α_i, is out of the valid range defined by (C2) and (C3), its value in the optimal solution of (P2'), denoted by α_i', is on the nearest boundary of the valid range, i.e., zero or P_t. Therefore, $\alpha_i'=\min[(|\alpha_i|+\alpha_i)/2,P_t]$.

Because UEs are not correlated with each other in this unconstrained problem (P2'), the above operation to α_i' will not affect other's optimal solution. After this process, (C2) and (C3) are satisfied. If (C1) is also satisfied, we conclude that this power allocation is the optimal solution to (P2) and $\alpha_i^*=\alpha_i', \ \forall i\in\mathbb{U}$.

If (C1) is not satisfied, it means that the back-haul capacity limit is violated. Due to the convexity of (P2), the optimal solution appears when the back-haul capacity is fully utilized by the front-hauls and thus (C1') is used to replace (C1). For this back-haul limited case, (P2) is converted to (P2'') as follows:

$$\begin{aligned}
&\max_{\boldsymbol{\alpha}} \ \sum_{i\in\mathbb{U}}[C(d_i,\alpha_i)+C(D_i,P_t-\alpha_i)], && \text{(P2'')}\\
&\textbf{s.t.} \ \text{(C1')}, \text{(C2)}, \text{(C3)}.
\end{aligned}$$

Substituting with (1), the Lagrange function is given by

$$\begin{aligned}
\mathcal{L}=&\sum_{i\in\mathbb{U}}\left[W\log_2(1+H_{di}\alpha_i)+W\log_2(1+H_{Di}(P_t-\alpha_i))\right]\\
&+\lambda_0\left[\sum_{i\in\mathbb{U}}W\log_2(1+H_{di}\alpha_i)-C'(D_x,P_t^F,\beta)\right]\\
&+\sum_{i\in\mathbb{U}}\mu_i\alpha_i+\sum_{i\in\mathbb{U}}\mu_{i+M}(P-\alpha_i).
\end{aligned} \qquad (5)$$

Taking a derivative of (5) w.r.t. α_i, and making it equal to zero, we have

$$(\lambda_0+1)\frac{H_{di}}{H_{di}\alpha_i+1}-\frac{H_{Di}}{H_{Di}(P_t-\alpha_i)+1}+\mu_i-\mu_{i+M}=0. \qquad (6)$$

According to the Karush-Kuhn-Tucker (KKT) conditions

$$\begin{aligned}
\mu_i\alpha_i&=0, \ \forall i\in\mathbb{U}\\
\mu_{i+M}(P_t-\alpha_i)&=0, \ \forall i\in\mathbb{U}\\
\mu_i&\ge 0, \ \forall i\in\mathbb{U}\\
\mu_{i+M}&\ge 0, \ \forall i\in\mathbb{U}.
\end{aligned} \qquad (7)$$

Therefore, when $\mu_{i+M}=0,\alpha_i=0\Longrightarrow\mu_i\ge 0$, the range of λ_0 can be found as follows:

$$\begin{aligned}
&\left[(\lambda_0+1)\frac{H_{di}}{H_{di}\alpha_i+1}-\frac{H_{Di}}{H_{Di}(P_t-\alpha_i)+1}\right]_{\alpha_i=0}\le 0\\
&\Longrightarrow \lambda_0\le\frac{H_{Di}}{(H_{Di}P_t+1)H_{di}}-1.
\end{aligned} \qquad (8)$$

Similarly, when $\mu_i = 0, \alpha_i = P_t \Longrightarrow \mu_{i+M} \geq 0$, the range of λ_0 can be obtained by

$$\begin{aligned} &\left[(\lambda_0+1)\frac{H_{di}}{H_{di}\alpha_i+1} - \frac{H_{Di}}{H_{Di}(P_t-\alpha_i)+1}\right]_{\alpha_i=P} \geq 0 \\ &\Longrightarrow \lambda_0 \geq \frac{(H_{di}P_t+1)H_{Di}}{H_{di}} - 1. \end{aligned} \tag{9}$$

When $\mu_i = \mu_{i+M} = 0 \Longrightarrow \alpha_i \in [0, P_t]$, α_i can be written as a function of λ_0 as follows:

$$\begin{aligned} &(\lambda_0+1)\frac{H_{di}}{H_{di}\alpha_i+1} - \frac{H_{Di}}{H_{Di}(P_t-\alpha_i)+1} = 0 \\ &= \alpha_i H_{di}H_{Di}(\lambda_0+2) + H_{Di} - (\lambda_0+1)(H_{Di}P_t+1)H_{di} \\ &\Longrightarrow \alpha_i = \frac{(\lambda_0+1)(H_{Di}P_t+1)H_{di} - H_{Di}}{H_{di}H_{Di}(\lambda_0+2)}. \end{aligned} \tag{10}$$

The range of λ_0 are determined by (8) and (9) to ensure that α_i is on the boundary of the valid range, i.e., α_i equals either 0 or P_t. We assume that the total number of UEs in $\mathbb{U}$ is M and the value range of λ_0 can be divided into $2M+1$ intervals by M UEs' boundaries. For the jth interval of λ_0, $\mathbb{R}_j$, we define the UEs that satisfy (8) belong to $\mathbb{U}_j^0$, and those satisfying (9) belong to $\mathbb{U}_j^P$.

When $\lambda_0 \in \mathbb{R}_j$, $\alpha_i, \forall i \in \mathbb{U}_j^0 \cup \mathbb{U}_j^P$, can be fixed as either 0 or P_t. The following constraints are used to replace the constraints (C2) and (C3) in (P2″)

$$\begin{aligned} &\alpha_i = 0, \forall i \in \mathbb{U}_j^0, \\ &\alpha_i = P_t, \forall i \in \mathbb{U}_j^P. \end{aligned} \tag{11}$$

The back-haul capacity should also be updated because it is deducted by the UEs whose power are fixed to P_t. The updated constraint (C1′) is given by

$$\begin{aligned} &\sum_{i\in\{\mathbb{U}-\mathbb{U}_j^0\cup\mathbb{U}_j^P\}} W\log_2(1+H_{di}\alpha_i) \\ &= C'(D_x, P_t^F, \beta) - \sum_{i\in\mathbb{U}_j^P} W\log_2(1+H_{di}P_t). \end{aligned} \tag{12}$$

We use (P2$_j$″) to denote the new problem where the constraints in (P2″) are updated as above.

Theorem 1. *The global maximizer of (P2$_j$″) is given by*

$$\begin{aligned} &\alpha_i = \frac{A(H_{Di}P_t+1)H_{di} - H_{Di}}{H_{di}H_{Di}}, \forall i \in \{\mathbb{U}-\mathbb{U}_j^0\cup\mathbb{U}_j^P\}, \\ &\alpha_i = 0, \forall i \in \mathbb{U}_j^0, \\ &\alpha_i = P_t, \forall i \in \mathbb{U}_j^P, \end{aligned} \tag{13}$$

where

$$A = \left[\left(\frac{2^{\frac{C'(D_x,P_t^F,\beta)-\sum_{i\in\mathbb{U}_j^P} W\log_2(1+H_{di}P_t)}{W}}}{\prod_{i\in\{\mathbb{U}-\mathbb{U}_j^0\cup\mathbb{U}_j^P\}}\frac{(H_{di}+H_{Di}+H_{di}H_{Di}P_t)}{H_{Di}}}\right)^{\frac{1}{M_j'}}\right]^+,$$

and M_j' is the total number of UEs in $\{\mathbb{U}-\mathbb{U}_j^0\cup\mathbb{U}_j^P\}$.

Proof. For $\alpha_i, \forall i \in \{\mathbb{U}-\mathbb{U}_j^0\cup\mathbb{U}_j^P\}$, it can be represented by (10). Substituting (10) into the updated constraint (12), we have

$$\begin{aligned} &\prod_{i\in\{\mathbb{U}-\mathbb{U}_j^0\cup\mathbb{U}_j^P\}} [1+H_{di}\alpha_i] \\ &= \prod_{i\in\{\mathbb{U}-\mathbb{U}_j^0\cup\mathbb{U}_j^P\}} \frac{(\lambda_0+1)(H_{di}+H_{Di}+H_{di}H_{Di}P_t)}{(\lambda_0+2)H_{Di}} \\ &= 2^{\frac{C'(D_x,P_t^F,\beta)-\sum_{i\in\mathbb{U}_j^P} W\log_2(1+H_{di}P_t)}{W}}. \end{aligned} \tag{14}$$

Given the total number of UEs in $\{\mathbb{U}-\mathbb{U}_j^0\cup\mathbb{U}_j^P\}$, M_j', (14) can be rewritten as

$$\begin{aligned} &\left(\frac{\lambda_0+1}{\lambda_0+2}\right)^{M_j'} \prod_{i\in\{\mathbb{U}-\mathbb{U}_j^0\cup\mathbb{U}_j^P\}} \frac{(H_{di}+H_{Di}+H_{di}H_{Di}P_t)}{H_{Di}} \\ &= 2^{\frac{C'(D_x,P_t^F,\beta)-\sum_{i\in\mathbb{U}_j^P} W\log_2(1+H_{di}P_t)}{W}}. \end{aligned} \tag{15}$$

$$\begin{aligned} \text{Define } A &= \left[\left(\frac{2^{\frac{C'(D_x,P_t^F,\beta)-\sum_{i\in\mathbb{U}_j^P} W\log_2(1+H_{di}P_t)}{W}}}{\prod_{i\in\{\mathbb{U}-\mathbb{U}_j^0\cup\mathbb{U}_j^P\}}\frac{(H_{di}+H_{Di}+H_{di}H_{Di}P_t)}{H_{Di}}}\right)^{\frac{1}{M_j'}}\right]^+ \\ &= \frac{\lambda_0+1}{\lambda_0+2}. \end{aligned} \tag{16}$$

Therefore, λ_0 can be obtained as follows:

$$\lambda_0 = \frac{2A-1}{1-A}. \tag{17}$$

By substituting the above result into (10) and combining with new constraints in (11), the optimal power allocation of (P2$_j$″) can be obtained. □

Given the optimal power allocation in Theorem 1, the system throughput assuming that λ_0 belongs to the jth interval, denoted by $C^{(j)}$, can be calculated by substituting the power allocation into the objective function of (P2″).

Given (17), we need to further check whether $\lambda_0 \in \mathbb{R}_j$. If λ_0 is out of the range of $\mathbb{R}_j$, the result contradicts with the settings of $\mathbb{U}_j^0$ and $\mathbb{U}_j^P$, so that there is no KKT point exists and λ_0 corresponding to the global maximizer of (P2″) cannot be in $\mathbb{R}_j$. We set $C^{(j)} = 0$ for this case. It should be noticed that for some of the intervals, $\mathbb{U}-\mathbb{U}_j^0\cup\mathbb{U}_j^P = \phi$ and $C'(D_x, P_t^F, \beta) - \sum_{i\in\mathbb{U}_j^P} W\log_2(1+H_{di}P_t) > 0$, or the deducted back-haul capacity is negative, or $\alpha_i \in (-\infty, 0]\cup[P_t, \infty), i \in \{\mathbb{U}-\mathbb{U}_j^0\cup\mathbb{U}_j^P\}$. These cases also mean that the KKT point does not exist in the current interval and we set $C^{(j)} = 0$ for these cases.

At most one KKT point can be found in each interval. If we add a minus to the objective function of (P2″), the Hessian matrix is positive definite. Thus, all the KKT points of (P2″) are either one of the local maximizers or the global maximizer. The KKT point corresponding to the maximum system throughput is the global maximizer. After we obtain $C^{(j)}$ for all the intervals, where $j = 1, 2, \ldots, 2M+1$, the maximum $C^{(j)}$ among all the intervals is the maximum system throughput of (P2″).

Remark 1. The global maximizer of (P2″) is obtained as follows:

$$\boldsymbol{\alpha}'' = \arg\max_{\boldsymbol{\alpha}} \left[C^{(1)}, C^{(2)}, \ldots, C^{(2M+1)} \right]. \tag{18}$$

Remark 2. The procedures of obtaining the optimal power allocation of (P2), $\boldsymbol{\alpha}^*$, given the location of the FR, can be summarized as:

(1) Solve (P2′) for each UE. Let $\alpha_i' = \min[(|\alpha_i| + \alpha_i)/2, P_t], \forall i \in \mathbb{U}$.
(2) Check whether the constraint (C1) is satisfied by $\boldsymbol{\alpha}'$.
- If so, $\boldsymbol{\alpha}^* = \boldsymbol{\alpha}'$;
- Otherwise, solve (P2$_j$″), $j = 1, 2, \ldots, 2M+1$, according to Theorem 1 and then obtain $\boldsymbol{\alpha}''$ based on Remark 1. $\boldsymbol{\alpha}^* = \boldsymbol{\alpha}''$.

5 3-D Placement Algorithm

5.1 Weighted Coordinate Axes (WCA)

In this section, the unpredictable network is assumed, i.e., we have no knowledge about how drastically and frequently the network changes. The FR's optimal location within 10-meter and 100-meter moving ranges may not be on the same path. Only the current information is applied to seek for a temporarily better location. Based on this instantaneous global information and the optimal power allocation given a fixed FR's location, we design the algorithms to determine the direction of the FR's next move.

We propose the Weighted Coordinate Axes algorithm inspired by the gradient ascent method. When the topology is stable, the FR shall move to a local maximizer as soon as possible. The gradient ascent method is a simple but effective way to find the local optimal point. The new location can be obtained based on the previous location as follows:

$$\boldsymbol{x}' = \boldsymbol{x} + R\nabla Z(\boldsymbol{x}), \tag{19}$$

where $\boldsymbol{x}$ and $\boldsymbol{x}'$ are the locations of the FR in the current step and the next step, respectively. R is the length of the step. $Z(\boldsymbol{x})$ denotes the maximum system throughput given the FR's location $\boldsymbol{x}$, which is obtained in Section 4.

Given that the gradient of $Z(\boldsymbol{x})$ is difficult to derive, we use numerical method to approximate the gradient of each step. It is first assumed that the FR moves along one of the 3-D axes toward positive and negative infinity for a short distance, Δ, respectively. The system throughput increments by these movements can be obtained. The difference between the throughput increments on two directions can be considered as the weight of this axis. The weighted sum of all the axes is the approximation of the gradient at the current location and results in the direction for the next step.

In a 3-D coordinate system, the weight of the x axis, w_1, is given by

$$w_1 = Z(\boldsymbol{x} + \Delta[1\ 0\ 0]) - Z(\boldsymbol{x} - \Delta[1\ 0\ 0]). \tag{20}$$

Similarly, w_2 and w_3 can be obtained. The direction of the FR's next step is given by $\boldsymbol{d} = [w_1\ w_2\ w_3]$.

A weight can be either positive or negative. A negative weight means that the system throughput is decreasing in that axis' positive direction. Based on the direction, $\boldsymbol{d}$, and the fixed step length, R, the coordinate of the FR in the next step, $\boldsymbol{x}'$, is obtained by

$$\boldsymbol{x}' = \boldsymbol{x} + \frac{R\boldsymbol{d}}{||\boldsymbol{d}||}. \tag{21}$$

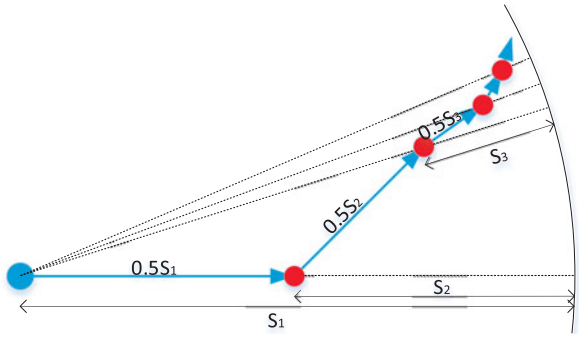

Fig. 2. An example of the adaptive step length.

The WCA algorithm can be extended to other cases. For example, in practice, the FR may be restricted to a certain height due to safety concerns. In this case, the dimension is reduced to 2-D. By applying the same method shown above but making $w_3 = 0$ in $\boldsymbol{d}$, the next step, $\boldsymbol{x}'$, can be obtained. When No-fly zones applied in practice, (21) should be further checked for each step to ensure $\boldsymbol{x}'$ is in the feasible region. In order to avoid zigzagging flight path, additional conditions can be added to stop the WCA algorithm. One feasible way is to calculate the throughput increment for each direction. For example, $I_1^+ = Z(\boldsymbol{x} + \Delta[1\ 0\ 0]) - Z(\boldsymbol{x})$ and $I_1^- = Z(\boldsymbol{x} - \Delta[1\ 0\ 0]) - Z(\boldsymbol{x})$ are the increments of the positive and negative directions on the x axis, respectively. If all the six increments along three axes are negative, the current location is almost on a local maximizer and the WCA algorithm stops.

5.2 Adaptive Weighted Coordinate Axes (A-WCA)

Besides the study on unpredictable network, we propose the A-WCA algorithm to deal with the predictable network, i.e., the network keeps stable for a certain time and this duration is predictable. Given the stable duration and the moving speed of the FR, the maximum number of steps and moving distance can be obtained. The objective of the A-WCA algorithm is to find the optimal location within a certain distance or a given number of steps.

Different from the one-step optimization in WCA, the FR moves to the target location directly after the A-WCA calculation. It means the FR does not move while the A-WCA's searching process. Thus, without the constraint of the FR's moving speed, an adaptive step length can be adopted to improve the efficiency, as shown in Fig. 2. Given the maximum moving distance, the minimum distance from the location of the ith step to the boundary, denoted as $S_i, i = 1, 2, \ldots$, can be obtained as follows:

$$S_i = \Phi - ||\boldsymbol{x}_{i-1} - \boldsymbol{x}_0||, \forall i > 0, \tag{22}$$

where Φ is the FR's maximum moving distance within the predicted network stable duration. $\boldsymbol{x}_i$ is the location at the ith step and $\boldsymbol{x}_0$ is the initial location.

The step length of the ith step is given by $R_i = S_i/2$. Specifically, $R_1 = S_1/2 = \Phi/2$. The coordinate updating equation in searching process is given by

$$\boldsymbol{x}_i = \boldsymbol{x}_{i-1} + \frac{(\Phi - ||\boldsymbol{x}_{i-1} - \boldsymbol{x}_0||)\boldsymbol{d}}{2||\boldsymbol{d}||}, \forall i > 0. \tag{23}$$

By applying the proposed A-WCA algorithm, the FR is guaranteed to stay within a sphere with radius Φ. The searching process will end when $R_i < \Gamma$, where Γ is a predetermined threshold.

If the A-WCA algorithm targets on a point on the spherical boundary, the step length decreases exponentially and the searching process stops quickly. However, when the algorithm targets on a local maximizer within the sphere, the A-WCA may never stop due to its fluctuating step length. We thereby need a mechanism to reduce the step length in this case. Similar to the pocket algorithm, we maintain the minimum distance from the searched location to the sphere boundary in the pocket during the searching process. Whenever there is a smaller distance generated by the new location, the distance in the pocket will be replaced. The step length is reduced by half if the pocket has not been updated for successive Λ steps. The detailed procedure of the A-WCA algorithm is summarized in Algorithm 1.

Algorithm 1. The A-WCA Algorithm

procedure A-WCA SEARCH
  Initialization:
  $i = 0$, $R_0 = \frac{\Phi}{2}$, Counter $= 0$, Pocket $= \Phi$, F = 0
  while $R_i \geq \Gamma$ **do**
    $i = i + 1$
    Update S_i and $\boldsymbol{x}_i$ according to (22) and (23)
    if F = 0 **then**
      $R_i = \frac{S_i}{2}$
    end if
    if $R_i <$ Pocket **then**
      Pocket = R_i, Counter = 0
    else
      Counter = Counter + 1
    end if
    if Counter $\geq \Lambda$ **then**
      $R_i = \frac{R_i}{2}$, F = 1
    end if
  end while
end procedure

5.3 Direct Method

To examine the WCA algorithm in terms of the convergence rate, we compare it with a direct off-line method. In this off-line method, we first obtain the location corresponding to the highest system throughput using the WCA algorithm within a certain steps, and then let the FR move to it directly along a straight line.

In practice, the direct off-line method is difficult to be applied because it significantly increases the computation load of the FR and the long-term prediction may not be accurate in dynamical networks. In the following performance analysis, we consider this method as an upper bound of the convergence rate for the WCA algorithm.

5.4 Dynamic Programming Method

In unpredictable networks, we want to examine how much accumulated throughput can be achieved before the next change. The accumulated throughput is given by $Acc(n) = \sum_{f=0}^{n}\sum_{i\in\mathbb{U}}\Big[C(||\boldsymbol{x}^f - \boldsymbol{u}_i||_2, \alpha_i^f) + C(||\boldsymbol{s}_i - \boldsymbol{u}_i||_2, P_t - \alpha_i^f)\Big]$, where $\boldsymbol{x}^f$ and α_i^f denote the location of the FR and the ith UE's power allocation in the fth step, respectively. The accumulated throughput includes every steps along the flight path starting from the 0th step (the initial location) to the nth step (the current location). For this metric, the Dynamic Programming (DP) is applied as a benchmark for comparison.

The DP is well known as a tool for the route optimization that provides the maximum utility [41]. However, it is suitable for the problems with discrete routing nodes. In this paper, the movements of the FR are not restricted between discrete points, which means that the number of routing nodes is infinite. To simplify the problem, we first build up a cuboid 3-D grid where the straight line connecting the initial location of the FR and the target location is the body diagonal.

We use $Z_{i,j,k}$ to denote the system throughput of the routing nodes (i, j, k) on the 3-D grid, which can be calculated as explained in Section 4. The routing nodes start from the node $(0, 0, 0)$, the initial location of the FR, and end at the target (I, J, K). There are $(I+1)(J+1)(K+1)$ nodes in total on the 3-D grid. $U^*_{i,j,k}$ denotes the maximum accumulated system throughput from $(0, 0, 0)$ to (i, j, k). The recursive equation is given by

$$U^*_{i,j,k} = \mathbf{max}\Big[U^*_{i-1,j,k}, U^*_{i,j-1,k}, U^*_{i,j,k-1}\Big] + Z_{i,j,k}, \quad \forall i \in [1, I], \forall j \in [1, J], \forall k \in [1, K]. \tag{24}$$

When any one or two variables in (i, j, k) equal zero, the recursive equation will be modified. For example, if $i = 0$

$$U^*_{0,j,k} = \mathbf{max}\Big[U^*_{0,j-1,k}, U^*_{0,j,k-1}\Big] + Z_{i,j,k}, \quad \forall j \in [1, J], \forall k \in [1, K]. \tag{25}$$

If $i = j = 0$

$$U^*_{0,0,k} = U^*_{0,0,k-1} + Z_{i,j,k}, \forall k \in [1, K]. \tag{26}$$

Other cases are similar. Besides that, we have $U^*_{0,0,0} = Z_{0,0,0}$.

Given the recursive equations above, the maximum accumulated system throughput at each routing node on the 3-D grid can be obtained. By the backward search from the target location and pick up the previous node corresponding to the maximum accumulated system throughput one by one, the optimal route is obtained. This route is denoted by a set of routing nodes' coordinates that it passes by, $\mathbb{H} : \{\boldsymbol{h}_1, \boldsymbol{h}_2, \ldots, \boldsymbol{h}_{I+J+K}\}$. $\boldsymbol{h}_1$ is the initial location of the FR and $\boldsymbol{h}_{I+J+K}$ is the destination. Every component in vector $\boldsymbol{h}_{I+J+K} - \boldsymbol{h}_s$ is equal to or greater than that in $\boldsymbol{h}_{I+J+K} - \boldsymbol{h}_{s+1}, \forall s \in [1, I + J + K - 1]$.

The route $\mathbb{H}$ goes along the 3-D grid and the distance between two adjacent routing nodes in $\mathbb{H}$ may not be the same as the step length of the FR. Therefore, we use the current location of the FR, $\boldsymbol{x}$, as the center to form a sphere, with a radius of step length R. Several intersections of this sphere and route $\mathbb{H}$ can be obtained and the one with the

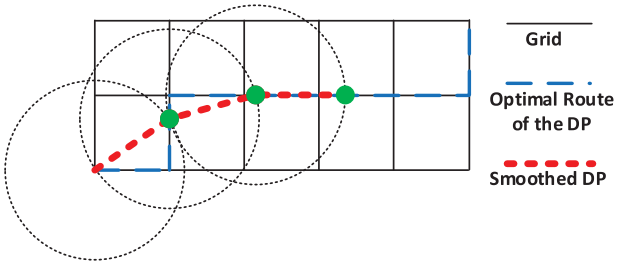

Fig. 3. An example the smoothed DP route.

shortest distance to the destination will be the location of the FR's next step. This route is considered as the Smoothed DP (SDP) route. A simple example in the 2-D plane can be found in Fig. 3.

6 Performance Analysis

6.1 One-Snapshot Simulation

A snapshot of random UE distribution (8 UEs) is shown in Fig. 4, the flight path of the FR obtained by the WCA algorithm is marked. It can be observed that after several steps of moving, the FR converges to one point. The flight path is close to that of the direct off-line method, as shown in the figure.

In this simulation, the bandwidth for each UE is $W = 1$ MHz, about 6 Physical Resource Blocks in the LTE system. The bandwidth for the FR is 5 times of UE's, i.e., $\beta = 5$. The maximum transmission powers are $P_t = 200$ mW and $P_t^F = 1000$ mW for the UE and the FR, respectively. The noise spectral density is $n_0 = 10^{-17.4}$ mW/Hz and $N_0 = Wn_0$. The NLOS channel in [42] is adopted, where $r = 3.68$, $K_0 = 10^{4.38}$. We do not consider the random shadowing in this case, thus $\Psi = 1$. The reference distance is $d_0 = 10$ m. Four fixed BSs' coordinates are $[500\ 500\ 500], [0\ 250\ 250], [500\ 0\ 0]$ and $[1000\ 0\ 250]$. Each axis of a UE's coordinate is randomly selected within $(0, 500)$. The initial location of the FR follows the same distribution. Because of the complexity of the radio bearer reconfiguration for the relay node, the FR cannot switch a serving BS dynamically. Therefore, in this paper, we assume a fixed serving BS for the FR, and the FR selects the nearest BS (based on FR's initial location) as its serving BS in the following simulations.

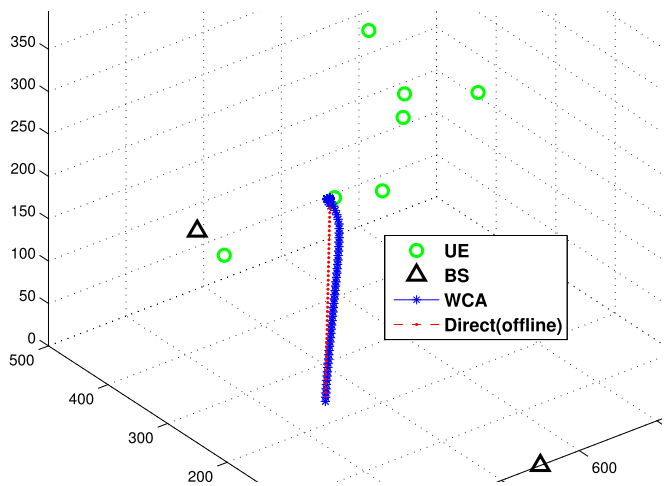

Fig. 4. An example of the FR's movement based on the WCA algorithm.

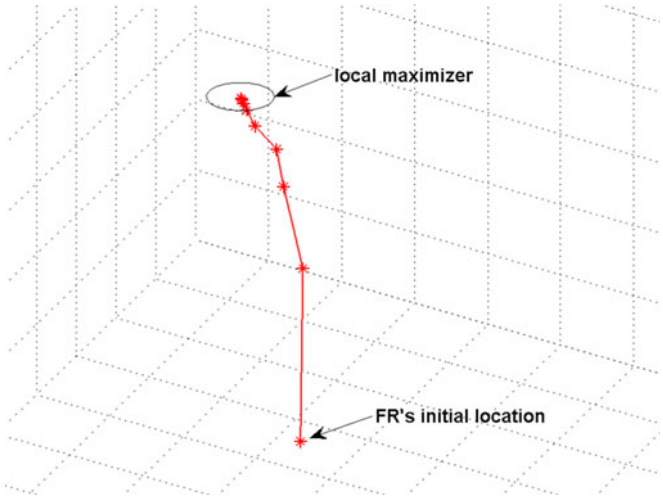

(a) Local optimal on the boundary

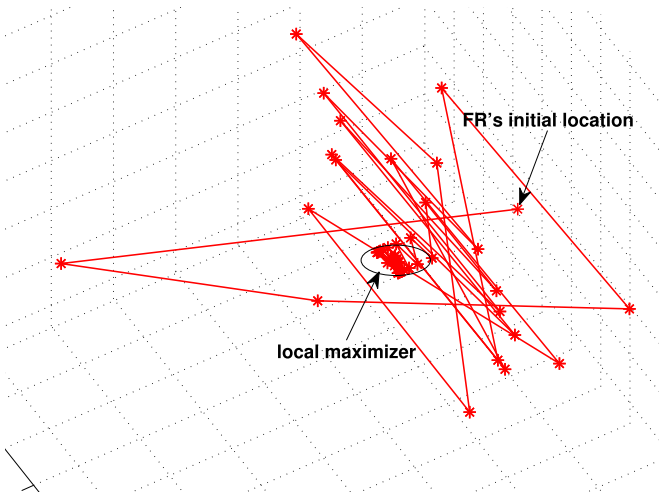

(b) Local optimal inside the feasible region

Fig. 5. Examples of the A-WCA's searching process.

Snapshots of the A-WCA's searching process given a stable duration of 30 seconds are shown in Fig. 5. The FR needs to find the optimal location within its maximum moving distance which is 30 meters assuming 1 m/s moving speed.

Fig. 5a is a typical case where the network's stable duration is relatively short and the FR has a limited moving distance. In this case, the FR has a higher chance to target on a maximizer outside the moving range, and finally it will stop at a point on the boundary after the A-WCA search. The step length decreases exponentially for most of the time and thus the process stops quickly. We set the threshold, $\Gamma = 0.1$ m, for the step length in the simulation. It takes 9 iterations in Fig. 5a to finish the searching.

When the stable duration is longer and can support the FR to move further, the FR is more possible to target on a maximizer within the maximum moving range as shown in Fig. 5b. Though fluctuating at the beginning, the searching trace can still converge to a local maximizer after reducing the step length by half several times compulsively according to Algorithm 1. Given $\Lambda = 5$ in the simulation, it takes 55 iterations in Fig. 5b to finish the searching. It should be noticed that the FR will fly to the converged local maximizer directly, rather than moving along the searching trace.

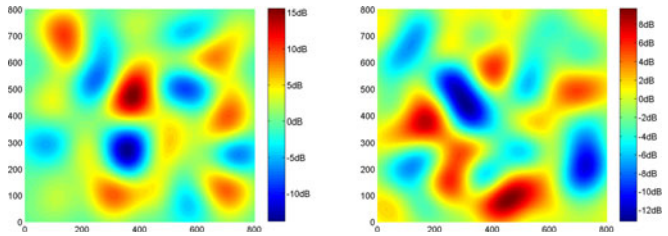

Fig. 6. Examples of the random shadowing map.

The NLOS path loss is applied in Fig. 4, which can be considered as the homogeneous shadowing case. In order to examine the proposed schemes in a harsher environment, a random shadowing is also adopted. We generate the shadowing map according to [43]. It follows Gaussian distribution in logarithmic scale with a standard deviation of 4 dB. We generate it for each UE because they have fixed locations while the FR is moving in the simulation. Considering the tower blocks in the city area, the shade mostly exists horizontally but not vertically so that the 2-D shadowing map is used in this paper. Examples of random shadowing map are shown in Fig. 6. UEs' shadowing maps are different, due to their locations, but highly correlated because they are blocked by the same building. We use two extreme cases, i.e., all the UEs share the identical shadowing map and each UE has an independent shadowing map, in the following simulations.

Given a predicted 30-second network stable duration, we apply the A-WCA algorithm successively for each 30-second period until reach a maximizer inside the feasible region (like the case in Fig. 5b) rather than on the boundary. The flight paths of the A-WCA and WCA algorithms are marked in Figs. 7a and 7b for the identical and the independent shadowing, respectively. Mostly, the two paths are consistent with each other in trend when using identical shadowing map, but they are likely to deviate and end up at different locations in the case of independent shadowing. $Z(\boldsymbol{x})$ becomes very rugged if users' shadowing are independent. Thus, the A-WCA algorithms is likely to climb toward a maximizer different from the WCA's target because of its long step length at the beginning of the searching process.

6.1.1 Convergence Rate

In Fig. 8, the system throughput on each step according to the flight path in Fig. 4 is shown and the comparison between the WCA algorithm and the direct off-line method are made for different step length settings. As shown in the figure, we choose $R = 3, 5, 10$, respectively. With the decreasing of the step length R, the gap between these two methods is slightly increased, but they are still very close to each other, which means that the convergence rate of the WCA algorithm is almost the same with that of the upper-bound (direct off-line method).

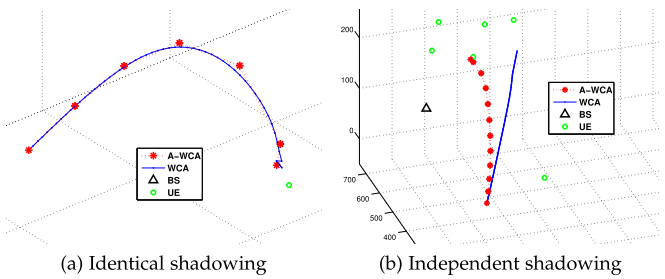

Fig. 7. Examples of the FR's movement based on the WCA and the A-WCA algorithms.

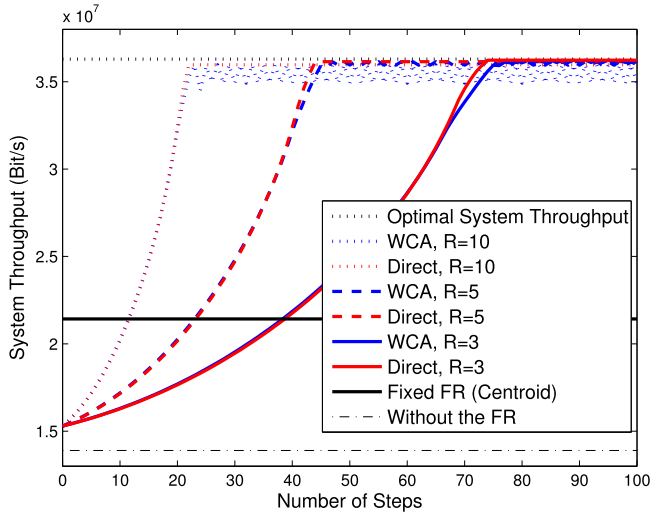

Fig. 8. Comparisons between the WCA and the optimal results, in terms of the convergence rate and the maximum system throughput (homogeneous shadowing).

A smaller step length will result in more steps to reach the maximum system throughput in Fig. 8. However, it will not lead to a longer time consumption in practice. In this simulation, the throughput reaches the maximum at the 79th, 47th and 23th step for the cases of $R = 3$, $R = 5$ and $R = 10$, respectively. Considering the step length, the actual moving distances of the FR are 237, 235 and 230 for the three cases. If the moving speed of the FR is constant, the time consumptions of different step lengths are similar.

The A-WCA's convergence rate is the upper-bound within a certain range because its flight path is a straight line within the maximum moving distance of the stable duration. It can be compared with the WCA if they target on the same maximizer. When the A-WCA is applied successively, the overall flight path is very close to that of the WCA, as shown in Fig. 7a. The system capacities along the paths are shown in Fig. 9a, and they have similar convergence rate. In Fig. 9, because of different step lengths, the time elapsing is adopted as the x-axis. In the random shadowing cases we also applied the condition mentioned in Section 5.1 to avoid the zigzagging flight path. By comparing with Fig. 8, we can observe that the fluctuation is mitigated in In Fig. 9.

6.1.2 Maximum System Throughput

Besides the convergence rate, we also examine how close the WCA algorithm can get to the optimal location (the optimal system throughput). The optimal system throughput is calculated by the exhaustive search method based on discrete points. All the points are on the intersections of a uniform 3-D grid and the side length of each cell is small enough (0.5 m).

It can be observed from Fig. 4 that the FR can converge to the vicinity of the optimal location and keep moving around it, which results in the zigzag in throughput curves in Fig. 8.

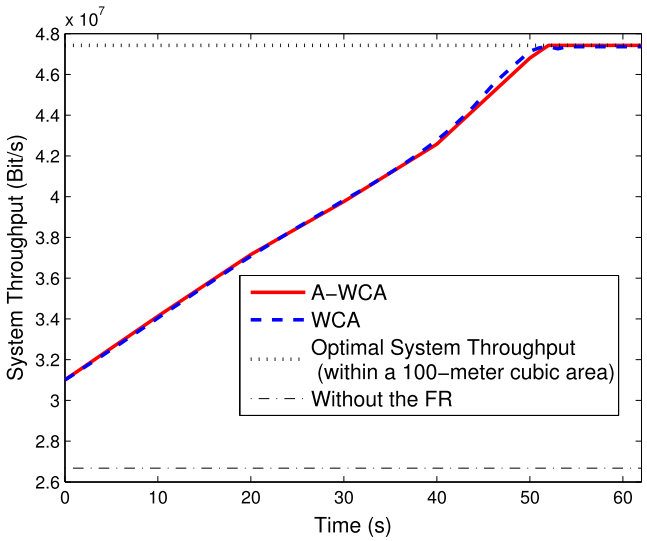

(a) Identical shadowing

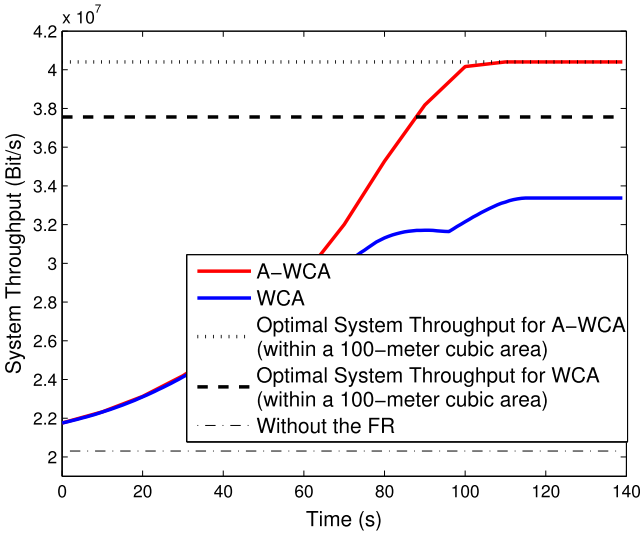

(b) Independent shadowing

Fig. 9. Comparisons between the WCA and the A-WCA.

We also use a fixed FR located at the centroid of the tetrahedron formed by four existing BSs, which intuitively is a good choice to add a new network node, as another benchmark. According to Fig. 8, this solution is far from what can be achieved by the proposed WCA algorithm.

From Fig. 8, when R is small, the FR can get closer to the optimal location and thus the maximum system throughput achieved by the WCA algorithm further approaches the optimal throughput. Based on the discussion above, a smaller step length can make the FR get closer to the optimal location and will not have a big impact on the convergence rate and time consumption, but a smaller step length will lead to a heavier computation load and increase the signaling/feedback load.

The A-WCA algorithm can achieve a better performance than the WCA for most of the time. When they target on the same maximizer, the A-WCA can get closer to it thanks to its smaller searching step length ($\Gamma = 0.1$ m in the simulation), comparing with the fixed step length of the WCA ($R = 3$ m in the simulation), and thus achieve a slightly higher system throughput as shown in Fig. 9a. If $Z(\boldsymbol{x})$ is very rugged such as the case of independent shadowing, the WCA may either be trapped by a local maximizer (R is too small) or converge slowly (R is too big). On the contrary, the A-WCA has a higher chance to jump out of a small maximizer and converge quickly to a larger one thanks to its adaptive step length in searching process.

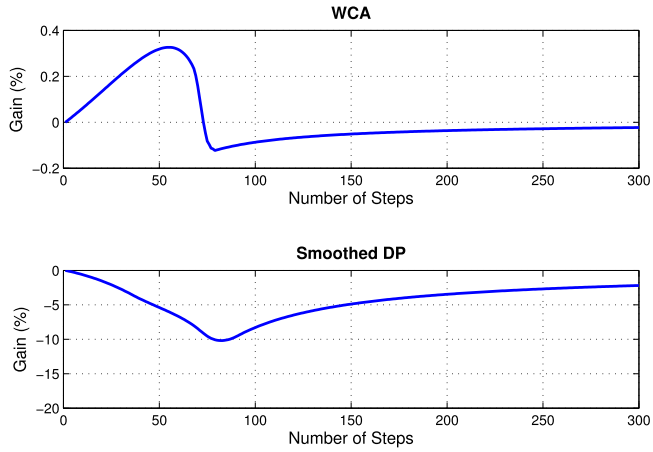

Fig. 10. Comparisons between the WCA, the smoothed DP, and the direct off-line schemes, in terms of accumulated throughput.

Fig. 9b shows the system throughput along the flight paths in Fig. 7b, and the A-WCA converges to a maximizer with a higher system throughput. Given the difficulty of finding the global optimal location when random shadowing is applied, we investigate whether the location achieved by the proposed algorithm is the global optimal within a 100-meter cubic area. Assuming that the algorithm achieved location is at (a, b, c), the 100-meter cubic area is $([a-50, a+50], [b-50, b+50], [c-50, c+50])$. The granularity of the exhaustive search in a 100-meter cubic area is 0.1 m. The figure shows that the A-WCA converges to a global maximizer within a 100-meter cubic area in this one-snapshot simulation but the WCA does not.

6.1.3 *Accumulated Throughput*

The same parameter settings for the one-snapshot simulation are applied to examine the accumulated throughput achieved by the proposed WCA algorithm. In this section, the direct off-line method is considered as the baseline. We introduce the gain as the metric which is defined as $\text{Gain}(n) = (Acc^{(*)}(n)/Acc_{direct}(n) - 1) \times 100\%$, where $Acc^{(*)}(n)$ denotes the accumulated throughput till the nth step of either the WCA algorithm or the SDP scheme, and $Acc_{direct}(n)$ is that of the direct off-line method.

In Fig. 10, it can be observed that the WCA algorithm can obtain a positive gain at the earlier stage. It is because in each step the FR moves toward the direction with a higher system throughput increment while the direct off-line method ignores the throughput of each step and results in a lower growth rate of the accumulated throughput at the beginning. Later on, the direct off-line method reaches the optimal location sooner than the WCA algorithm, and thus its growth rate will be higher than that of the WCA algorithm. This period corresponds to the sharp decreasing of the gain in Fig. 10. After the WCA reaches the peak, the growth rates of the two methods are the same. The gain will slowly converge to zero with the increasing number of steps.

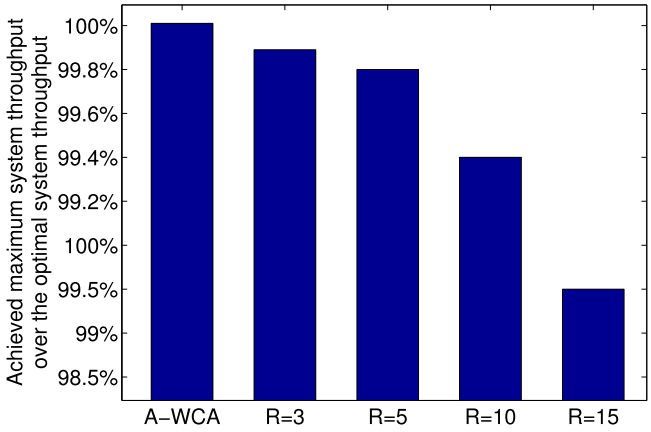

Fig. 11. Comparisons between the WCA and the optimal system throughput given the homogeneous shadowing.

On the contrary, the SDP cannot obtain a positive gain in this particular one-snapshot simulation. The main disadvantage of the DP is that it is originally designed based on the discrete points on the 3-D grid, which makes the total length of the route (flight path) much longer than that of the other two methods. A longer moving distance reduces the growth rate of the accumulated throughput and thus leads to the performance degradation. The one-snapshot simulation is conducted given the homogeneous shadowing. More cases will be considered in Monte Carlo simulations.

We do not investigate the A-WCA's performance in term of the accumulated throughput, because it is only meaningful when the A-WCA and WCA are targeting on the same maximizer and the A-WCA is equivalent to the direct offline method in this case. Otherwise, it will be more valuable to examine the maximum system throughput, i.e., which one can find a maximizer with a higher system throughput, rather than the accumulated throughput along the path.

6.2 Monte Carlo Simulation

6.2.1 Maximum System Throughput

Additional Monte Carlo simulations were conducted to further examine the gap between the maximum value obtained from the proposed algorithms and the optimal result. Four fixed BSs' coordinates are $[500\ 500\ 500], [500\ 0\ 0], [0\ 500\ 0]$ and $[0\ 0\ 500]$. The value of each axis in UE's coordinate is a random variable and follows the uniform distribution within $(0, 500)$. The initial location of the FR follows the same distribution.

In Fig. 11, given homogeneous shadowing, the system throughput achieved by the A-WCA and WCA algorithms over the optimal one are shown. We set a 30-second stable duration for the A-WCA algorithm, and different step lengths are applied for the WCA algorithm. The results are the average over 100 rounds of random Monte Carlo simulations. Due to the complexity of the exhaustive search for the optimal system throughput, the number of rounds cannot be too large, but they are sufficient to reveal the trends. Fig. 11 shows that by applying the WCA algorithm, the FR can be very close to the optimal location and achieve near-optimal system throughput. With the increasing of the step length, the gap between the WCA algorithm and the optimal throughput will increase. The A-WCA can achieve a better performance thanks to its smaller searching step length ($\Gamma = 0.1$ m in the simulation). The A-WCA's result is even higher than the optimal result (the exhaustive search) because of the coarse granularity of the exhaustive search (0.5 m).

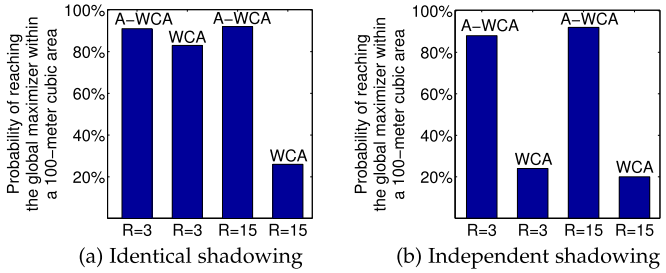

Fig. 12. Comparisons between the WCA and the A-WCA.

Both the A-WCA and WCA algorithms can converge to the global optimal location in most of the cases when homogeneous shadowing is applied. However, it is difficult in the random shadowing case due to the ruggedness of $Z(\boldsymbol{x})$. We investigate how possible the proposed algorithms can find a global maximizer within a 100-meter cubic area. We define a successful case as the location obtained by the algorithm is within 5 m from the optimal location. The results of 100-round Monte Carlo simulations are summarized in Fig. 12.

Fig. 12a is the identical shadowing case. We apply different step length R for the WCA algorithm and assume a $10R$ maximum moving distance for the A-WCA. The A-WCA is applied successively until reach a maximizer inside the feasible region rather than on the boundary. We can observe that the A-WCA can always achieve a better performance thanks to its adaptive step length of the searching process. It allows the A-WCA to jump out of a local maximizer and then converge quickly to a better one. This observation is consistent with that of the one-snapshot simulation. Besides, the A-WCA becomes slightly better when we increase the maximum moving distance or the network's stable duration. It is because the initial step length of the searching process is related to the maximum moving range. With a larger step, it will have a lower chance to be trapped in a local maximizer. The WCA algorithm is close to the A-WCA when $R = 3$, but deteriorates significantly when R is larger because it is difficult to converge given a fixed large step length.

In the independent shadowing case, the results of the A-WCA have the same trend but the WCA becomes worse, as shown in Fig. 12b. Reducing the step length is not very helpful for the WCA algorithm given $Z(\boldsymbol{x})$ is extremely rugged. The FR is easy to be misled by local maximizers and failed to converge to the global optimal location in certain area.

It can be concluded that when $Z(\boldsymbol{x})$ is smooth, such as the homogeneous and identical shadowing cases, the WCA algorithm can achieve a similar performance to the A-WCA's by wisely choosing the step length. The knowledge of the network's changing will not greatly improve the performance in these scenarios. In the independent shadowing case where $Z(\boldsymbol{x})$ is very rugged, the A-WCA shows a significant advantage. Thus, collecting the statistic information and predicting the network's changing pattern is necessary.

In Monte Carlo simulations, we only study the A-WCA in term of the maximum system throughput, i.e., whether it

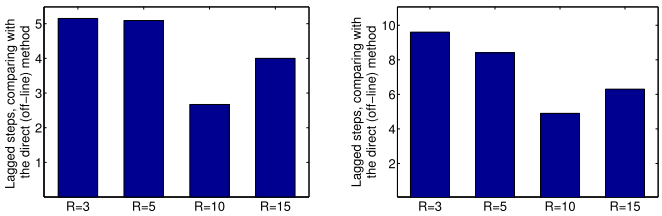

(a) Homogeneous shadowing (b) Independent shadowing

Fig. 13. Comparisons between the WCA and the direct off-line method, in terms of step number needed to reach the peak.

can find the optimal location within a 100-meter cubic area, especially in the random shadowing case. The convergence rate and the accumulated throughput are meaningful only if the A-WCA and the WCA target on the same maximizer. When the network's stable duration is short, the A-WCA's flight path is close to the WCA's. Otherwise, it gets closer to the direct off-line method. We can gain the insight on the A-WCA from the studies toward the WCA and the direct off-line method. Therefore, we mainly focus on the WCA algorithm in the following Monte Carlo simulations.

6.2.2 Convergence Rate

We use Monte Carlo simulations to verify the observation of convergence rate in the previous one-snapshot simulation. Fig. 13 shows how many extra steps are needed on average for the WCA algorithm to reach 99 percent of the maximum system throughput of the direct off-line method. It should be noticed that the WCA algorithm may reach the peak sooner than the direct off-line method. In these cases, the number of extra steps is set to zero.

As shown in Fig. 13a, the WCA algorithm only lags behind the off-line method for several steps given the homogeneous shadowing, which is consistent with the observation in Fig. 8. With the increase of step length, the lags decrease in most of the cases. The same trend can be observed in Fig. 13b, where the independent shadowing is applied. The WCA's flight path becomes circuitous in this case, which results in larger lags.

In both of the cases, when the step length is too big ($R = 15$ in the figure), the lag will increase. It is because the location of the FR fluctuates sharply when the step length is too large, which makes it difficult to converge to the target location. An example is shown in Fig. 14b. By comparing with the case of a smaller step length, it is difficult for the FR to converge when $R = 15$.

6.2.3 Accumulated Throughput

In this section, we further verify the range of the gain of the accumulated throughput defined in Section 6.1.3. In the one-snapshot simulation shown in Fig. 10, the maximum and minimum gains can be identified. We record both of them for the WCA algorithm and the SDP method, respectively, in each simulation round, and then take the average. The results are summarized in Table 1.

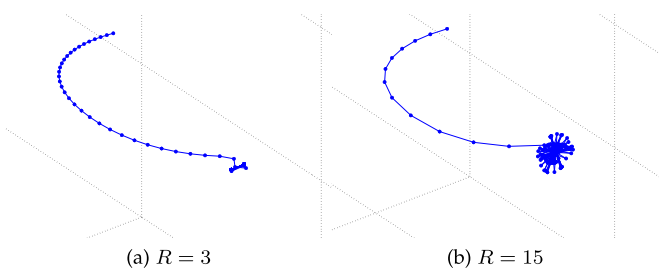

(a) $R = 3$ (b) $R = 15$

Fig. 14. An example of the WCA's flight path when $R = 3, 15$.

TABLE 1
The Range of the Gain

Algorithm	WCA	SDP
Maximum Gain (Averaged over 100 rounds) Homogeneous shadowing	1.95%	0.80%
Minimum Gain (Averaged over 100 rounds) Homogeneous shadowing	−0.82%	−3.38%
Maximum Gain (Averaged over 100 rounds) Independent shadowing	1.03%	0.61%
Minimum Gain (Averaged over 100 rounds) Independent shadowing	−2.77%	−2.98%

As shown in Table 1, the WCA algorithm can achieve a better performance than the SDP method. In the homogeneous shadowing case, if the network changes frequently (limited steps with a valid global information), the WCA algorithm can obtain a positive gain, which is less than 1.95 percent on average. Otherwise, the WCA slightly lose the accumulated throughput, less than 0.82 percent on average, comparing with the direct off-line method. The performance is worse in the independent shadowing case because of more circuitous flight path and the longer delay shown in Fig. 13.

According to the simulation results, we can conclude that, no matter how long the global information is valid, the WCA algorithm is as good as or even better than the offline schemes from the perspective of the accumulated throughput.

7 Future Work

Many open research issues are beckoning further studies. In this paper, we tried to find the optimal location for the FR to maximize the system throughput. The fairness among users was not considered, which is an important issue and given the channel dynamics, there exists a trade-off between overall throughput and fairness. Fairness can be considered by defining a utility function as the product of each user's throughput, or as the summation of a log function of each user's throughput. The proposed approach can be applied to maximize the utility to make a trade-off between the total throughput and fairness.

Another issue is the traffic model. In this paper, we use the sum of the Shannon capacities of all the UEs' front-haul links and serving links to approximate the system throughput. The capacity may be achieved only if the traffic is the full-buffer type. The users' buffer status should be further considered. The system can also be optimized based on the delay tolerance of the traffic with the constraint of the FR's speed limit.

The energy consumption combining with the solar-powered UAV in another important further research issue. The FR will not sit on one single optimal location. Instead, it should cruise along an optimized closed route. Given the solar charging rate varies in different areas, the proportion of the route within the high charging rate area should be above a threshold to guarantee the sustainability. With this new constraint, an optimization problem can be formulated.

Finally, we assumed that the FR is connected to a fixed serving BS in this paper. An optimized handover triggering mechanism enabled by the cooperation between existing stationary BSs will further improve the system performance.

8 Conclusion

In this paper, considering the high penetration loss/deep shadowing channels of the indoor users, we introduced the FR into the cellular system to improve the transmission efficiency and maximize the system throughput. Given the capacity limit of the FR's back-haul link and the maximum transmission power of each user, an optimization problem has been formulated to maximize the system throughput. The optimal power allocation strategy has been derived, and two effective online FR placement algorithms, i.e., the WCA for the unpredictable network and the A-WCA targeting on the predictable network, have been proposed. Two comparative off-line schemes, i.e., the direct and the SDP methods, have also been described.

Extensive simulations have been conducted. The results show that the WCA algorithm can reach the near-optimal system throughput given the homogeneous shadowing and can find the global optimal location within a certain range for most of the identical shadowing cases. Collecting the statistic information and predicting the network's changing pattern is desirable in the independent shadowing case, where the WCA is easily misled by local maximizers and the A-WCA shows a significant advantage thanks to its adaptive step length in the searching process.

More simulations focusing on the WCA algorithm have been included. When the homogeneous shadowing is applied, the convergence rate of the WCA algorithm is close to the upper-bound and its accumulated throughput along the flight path is as good as or even better than the offline schemes. However, the WCA's performance is worse in the independent shadowing case, which provides an insight on how the performance varies according to the ruggedness of the maximum system throughput over a 3-D area. It can be considered as the reference to determine the necessity of introducing the network prediction and the A-WCA algorithm.

Acknowledgments

This work was supported in part by the Natural Sciences and Engineering Research Council of Canada.

References

[1] K. Haneda, L. Tian, H. Asplund, J. Li, Y. Wang, D. Steer, C. Li, T. Balercia, S. Lee, Y. Kim, et al., "Indoor 5G 3GPP-like channel models for office and shopping mall environments," in *Proc. IEEE Int. Conf. Commun. Workshops*, 2016, pp. 694–699.

[2] 3GPP, "Study on 3D channel model for LTE; Release 12," 3rd Generation Partnership Project (3GPP), TR 36.873, 2017.

[3] B. Saha, E. Koshimoto, C. C. Quach, E. F. Hogge, T. H. Strom, B. L. Hill, S. L. Vazquez, and K. Goebel, "Battery health management system for electric UAVs," in *Proc. IEEE Aerosp. Conf.*, 2011, pp. 1–9.

[4] C. D. Gavrilovich, "Mobile communication system with moving base station," U.S. Patent 5 729 826, Mar. 17, 1998.

[5] Google. Project loon. 2016. [Online]. Available: http://www.google.com/loon/

[6] M. Zuckerberg. The technology behind aquila. 2016. [Online]. Available: https://www.facebook.com/notes/mark-zuckerberg/the-technology-behind-aquila/10153916136506634/

[7] R. Kirichek, A. Paramonov, and A. Koucheryavy, "Flying ubiquitous sensor networks as a queueing system," in *Proc. IEEE Int. Conf. Adv. Commun. Technol.*, 2015, pp. 127–132.

[8] A. Alkesh, A. K. Singh, and N. Purohit, "A moving base station strategy using fuzzy logic for lifetime enhancement in wireless sensor network," in *Proc. IEEE Int. Conf. Commun. Syst. Netw. Technol.*, 2011, pp. 198–202.

[9] Y. Yun and Y. Xia, "Maximizing the lifetime of wireless sensor networks with mobile sink in delay-tolerant applications," *IEEE Trans. Mobile Comput.*, vol. 9, no. 9, pp. 1308–1318, Sep. 2010.

[10] J. Luo, J. Panchard, M. Piórkowski, M. Grossglauser, and J.-P. Hubaux, "MobiRoute: Routing towards a mobile sink for improving lifetime in sensor networks," in *Proc. Int. Conf. Distrib. Comput. Sensor Syst.*, 2006, pp. 480–497.

[11] X. Xu, J. Luo, and Q. Zhang, "Delay tolerant event collection in sensor networks with mobile sink," in *Proc. IEEE INFOCOM*, 2010, pp. 1–9.

[12] M. Abo-Zahhad, S. M. Ahmed, N. Sabor, and S. Sasaki, "Mobile sink-based adaptive immune energy-efficient clustering protocol for improving the lifetime and stability period of wireless sensor networks," *IEEE Sens. J.*, vol. 15, no. 8, pp. 4576–4586, Aug. 2015.

[13] J. Pan, L. Cai, Y. T. Hou, Y. Shi, and S. X. Shen, "Optimal base-station locations in two-tiered wireless sensor networks," *IEEE Trans. Mobile Comput.*, vol. 4, no. 5, pp. 458–473, Sep./Oct. 2005.

[14] I. Chatzigiannakis, A. Kinalis, and S. Nikoletseas, "Efficient data propagation strategies in wireless sensor networks using a single mobile sink," *Comput. Commun.*, vol. 31, no. 5, pp. 896–914, 2008.

[15] L. He, Z. Yang, J. Pan, L. Cai, J. Xu, and Y. J. Gu, "Evaluating service disciplines for on-demand mobile data collection in sensor networks," *IEEE Trans. Mobile Comput.*, vol. 13, no. 4, pp. 797–810, Apr. 2014.

[16] M. Akbar, N. Javaid, A. H. Khan, M. Imran, M. Shoaib, and A. Vasilakos, "Efficient data gathering in 3D linear underwater wireless sensor networks using sink mobility," *Sens.*, vol. 16, no. 3, 2016, Art. no. 404.

[17] Y. Zhang, S. He, and J. Chen, "Near optimal data gathering in rechargeable sensor networks with a mobile sink," *IEEE Trans. Mobile Comput.*, vol. 16, no. 6, pp. 1718–1729, Jun. 2017.

[18] I. Bekmezci, O. K. Sahingoz, and Ş. Temel, "Flying ad-hoc networks (FANETs): A survey," *Ad Hoc Netw.*, vol. 11, no. 3, pp. 1254–1270, 2013.

[19] S. Gao, H. Zhang, and S. K. Das, "Efficient data collection in wireless sensor networks with path-constrained mobile sinks," *IEEE Trans. Mobile Comput.*, vol. 10, no. 4, pp. 592–608, Apr. 2011.

[20] A. Jimenez-Pacheco, D. Bouhired, Y. Gasser, J.-C. Zufferey, D. Floreano, and B. Rimoldi, "Implementation of a wireless mesh network of ultra light MAVs with dynamic routing," in *Proc. IEEE Globecom Workshops*, 2012, pp. 1591–1596.

[21] SenseFly. eBee. 2016. [Online]. Available: https://www.sensefly.com/drones/ebee.html

[22] D. Shallcross and E. van den Berg, "Autonomous location of mobile wireless relay nodes," in *Proc. IEEE Int. Conf. Unmanned Aircraft Syst.*, 2016, pp. 15–24.

[23] E. P. de Freitas, T. Heimfarth, I. F. Netto, C. E. Lino, C. E. Pereira, A. M. Ferreira, F. R. Wagner, and T. Larsson, "UAV relay network to support WSN connectivity," in *Proc. IEEE Int. Congr. Ultra Modern Telecommun. Control Syst.*, 2010, pp. 309–314.

[24] Y. Li and L. Cai, "UAV-assisted dynamic coverage in a heterogeneous cellular system," *IEEE Netw.*, vol. 31, no. 4, pp. 56–61, Jul./Aug. 2017.

[25] C. Mukasa, V. A. Aalo, and G. Efthymoglou, "On the performance of a dual-hop network with a mobile relay in a Nakagami fading environment," in *Proc. IEEE 21st Int. Workshop Comput. Aided Model. Des. Commun. Links Netw.*, 2016, pp. 43–47.

[26] J. Lyu, Y. Zeng, and R. Zhang, "Cyclical multiple access in UAV-aided communications: A throughput-delay tradeoff," *IEEE Wireless Commun. Lett.*, vol. 5, no. 6, pp. 600–603, Dec. 2016.

[27] Y. Zeng, R. Zhang, and T. J. Lim, "Wireless communications with unmanned aerial vehicles: Opportunities and challenges," *IEEE Commun. Mag.*, vol. 54, no. 5, pp. 36–42, May 2016.

[28] I. Bor-Yaliniz and H. Yanikomeroglu, "The new frontier in RAN heterogeneity: Multi-tier drone-cells," *IEEE Commun. Mag.*, vol. 54, no. 11, pp. 48–55, Nov. 2016.

[29] M. Alzenad, A. El-Keyi, F. Lagum, and H. Yanikomeroglu, "3D placement of an unmanned aerial vehicle base station (UAV-BS) for energy-efficient maximal coverage," *IEEE Wireless Commun. Lett.*, vol. 6, no. 4, pp. 434–437, Aug. 2017.

[30] R. I. Bor-Yaliniz, A. El-Keyi, and H. Yanikomeroglu, "Efficient 3-D placement of an aerial base station in next generation cellular networks," in *Proc. IEEE Int. Conf. Commun. Workshops*, 2016, pp. 1–5.
[31] M. Mozaffari, W. Saad, M. Bennis, and M. Debbah, "Efficient deployment of multiple unmanned aerial vehicles for optimal wireless coverage," *IEEE Commun. Lett.*, vol. 20, no. 8, pp. 1647–1650, Aug. 2016.
[32] M. Mozaffari, W. Saad, M. Bennis, and M. Debbah, "Unmanned aerial vehicle with underlaid device-to-device communications: Performance and tradeoffs," *IEEE Trans. Wireless Commun.*, vol. 15, no. 6, pp. 3949–3963, Jun. 2016.
[33] E. Kalantari, M. Z. Shakir, H. Yanikomeroglu, and A. Yongacoglu, "Backhaul-aware robust 3D drone placement in 5G+ wireless networks," in *Proc. IEEE Int. Conf. Commun. Workshops*, 2017, pp. 109–114.
[34] M. Mozaffari, W. Saad, M. Bennis, and M. Debbah, "Mobile internet of things: Can UAVs provide an energy-efficient mobile architecture?" in *Proc. IEEE Global Commun. Conf.*, 2016, pp. 1–6.
[35] M. Mozaffari, W. Saad, M. Bennis, and M. Debbah, "Mobile unmanned aerial vehicles (UAVs) for energy-efficient internet of things communications," *IEEE Trans. Wireless Commun.*, vol. 16, no. 11, pp. 7574–7589, Nov. 2017.
[36] Y. Zeng and R. Zhang, "Energy-efficient UAV communication with trajectory optimization," *IEEE Trans. Wireless Commun.*, vol. 16, no. 6, pp. 3747–3760, Jun. 2017.
[37] Y. Zeng, R. Zhang, and T. J. Lim, "Throughput maximization for UAV-enabled mobile relaying systems," *IEEE Trans. Commun.*, vol. 64, no. 12, pp. 4983–4996, Dec. 2016.
[38] S. Rohde, M. Putzke, and C. Wietfeld, "Ad hoc self-healing of OFDMA networks using UAV-based relays," *Ad Hoc Netw.*, vol. 11, no. 7, pp. 1893–1906, 2013.
[39] 3GPP, "Further advancements for E-UTRA physical layer aspects; Release 9," 3rd Generation Partnership Project (3GPP), TR 36.814, 2017.
[40] S. Boyd and L. Vandenberghe, *Convex Optimization*. Cambridge, U.K.: Cambridge Univ. Press, 2004.
[41] P. MohajerinEsfahani, D. Chatterjee, and J. Lygeros, "Motion planning for continuous time stochastic processes: A dynamic programming approach," *IEEE Trans. Autom. Control*, vol. 61, no. 8, pp. 2155–2170, Aug. 2016.
[42] C. Xu, L. Song, and Z. Han, *Resource Management for Device-to-Device Underlay Communication*. Berlin, Germany: Springer, 2014.
[43] I. Forkel, M. Schinnenburg, and M. Ang, "Generation of two-dimensional correlated shadowing for mobile radio network simulation," in *Proc. Int. Symp. Wireless Personal Multimedia Commnu.*, Sep. 2004, Art. no. 43.

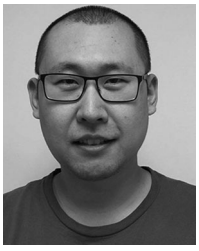

Yue Li received the BSc and MSc degrees in electrical engineering from the Beijing Institute of Technology, Beijing, China, in 2006 and 2008, respectively. He is working toward the PhD degree in the Department of Electrical and Computer Engineering, University of Victoria, Victoria, Canada. During 2008-2013, he worked for Huawei as a standard pre-research engineer with the Wireless Research Department. He has been closely involved in 3GPP standards evolvement and held numerous patents in WCMDA, LTE-A, and 5G systems. His research interests include next-generation cellualr system, wireless network design and optimization, wireless system modeling, and performance analysis.

Guangsheng Feng received the BE degree from Harbin Engineering University (HEU), in 2003, the ME degree from the Harbin Institute of Technology (HIT), in 2005, and the PhD degree from Harbin Engineering University, in 2009. He is currently a associate professor with the Department of Computer Science and Technology, HEU, and his research interests involve mobile edge computing, access control, and multimedia transmission in wireless networks.

Mohammad Ghasemiahmadi received the BSc and MASc degrees in electrical engineering with a minor in telecommunications from the University of Tehran, Tehran, Iran, in 2015, and from the Department of Electrical and Computer Engineering, University of Victoria, Victoria, Canada, in 2018, respectively. His research interests include physical layer networking, machine to machine communication and next-generation cellular systems, software defined radio, and protocol implementation. Currently, he is a test automation agile team member with Schneider Electric.

Lin Cai (S'00-M'06-SM'10) received the MASc and PhD degrees in electrical and computer engineering from the University of Waterloo, Waterloo, Canada, in 2002 and 2005, respectively. Since 2005, she has been with the Department of Electrical & Computer Engineering, University of Victoria, and she is currently a professor. Her research interests span several areas in communications and networking, with a focus on network protocol and architecture design supporting emerging multimedia traffic over wireless, mobile, ad hoc, and sensor networks. She has served as a TPC symposium co-chair for IEEE Globecom'10 and Globecom'13. She served as an associate editor of the *IEEE Transactions on Wireless Communications*, the *IEEE Transactions on Vehicular Technology*, the *EURASIP Journal on Wireless Communications and Networking*, the *International Journal of Sensor Networks*, and the *Journal of Communications and Networks* (JCN), and as the distinguished lecturer of the IEEE VTS Society. She was a recipient of the NSERC Discovery Accelerator Supplement Grants in 2010 and 2015, respectively, and the Best Paper Awards of IEEE ICC 2008 and IEEE WCNC 2011. She has founded and chaired the IEEE Victoria Section Vehicular Technology and Communications Joint Societies Chapter. She is a senior member of the IEEE.